



# Seismic $b$ -value reduction prior to the 28th April 2021, $M_w$ 6.5 Sonitpur earthquake of Assam Valley

BANASHREE SARMA<sup>1</sup>, KAJALJYOTI BORAH<sup>1,2,\*</sup> , DIPOK K BORA<sup>3,4</sup> and  
AAKASH ANAND<sup>1</sup>

<sup>1</sup>Department of Earth Sciences, IISER Kolkata, Mohanpur 741 246, West Bengal, India.

<sup>2</sup>Center for Climate and Environmental Studies, IISER Kolkata, Mohanpur 741 246, West Bengal, India.

<sup>3</sup>Department of Physics, Diphu Government College, Diphu, Karbi Anglong 782 462, Assam, India.

<sup>4</sup>Government Model College, Deithor, Karbi Anglong 782 480, Assam, India.

\*Corresponding author. e-mail: kajal.borah@iiserkol.ac.in

MS received 18 August 2021; revised 18 April 2022; accepted 19 April 2022

The Kopili Fault is one of the most active faults in northeast India, which is the causative source of several earthquakes. The zone is of great importance to the scientific community because of its seismic productivity in past as well in present, which includes two major earthquakes ( $M > 7$ ), several moderate earthquakes, and most recent 28th April 2021  $M_w$  6.5 earthquake. In the present study, shear velocity crustal structure is mapped and the  $b$ -value is calculated near the Kopili Fault region using receiver function modelling and Gutenberg–Richter relation, respectively. Joint inversion of receiver function and Rayleigh wave group velocity dispersion data beneath Tezpur (TZR) station shows 40 km thick crust with 18 km upper and 22 km lower crust. However, thin crust (35 km) is observed beneath Mikir Hills. The overall  $b$ -value in the Kopili region is estimated to be 0.94. We observed an increase in  $b$ -value with depths, which may be due to the strength of crust and upper mantle material caused by the rise in temperature and pressure. The  $b$ -value variation with depth shows a sudden increase of  $b$ -value at a depth of 40–45 km, which corresponds to the crust–mantle transition, estimated from the receiver function modelling in the region. A sudden reduction of  $b$ -value is observed prior to 28th April 2021  $M_w$  6.5 earthquake, which underscores investigations of the  $b$ -value and its variations for the purpose of earthquake precursor studies in that area.

**Keywords.** Kopili Fault; inversion;  $b$ -value; crustal structure; Deming regression; bootstrap.

## 1. Introduction

Northeast India is one of the most diverse, tectonically complex, earthquake-prone regions in the Indian subcontinent, which has experienced two great earthquakes, *viz.*, the Shillong earthquake (12th June 1897) of magnitude  $M_w$  8.1 and the Assam earthquake (15th August 1950) of magnitude  $M_w = 8.4$  (Bilham and England 2001; Ambraseys and Douglas 2004) and more than 20

large earthquakes of magnitude  $>7.0$ . The region consists of distinct geological blocks, *viz.*, the eastern Himalaya, Shillong Plateau, Mikir Hills, Assam Valley, Bengal Basin, and Indo Burma subduction zone (figure 1). The Assam Valley is the narrowest valley (width  $<50$  km) in the region that sits immediately north of Shillong Plateau. The Shillong Plateau is separated from the Mikir Hills and Bengal Basin by the NW–SE trending Kopili Fault to the east and the EW trending

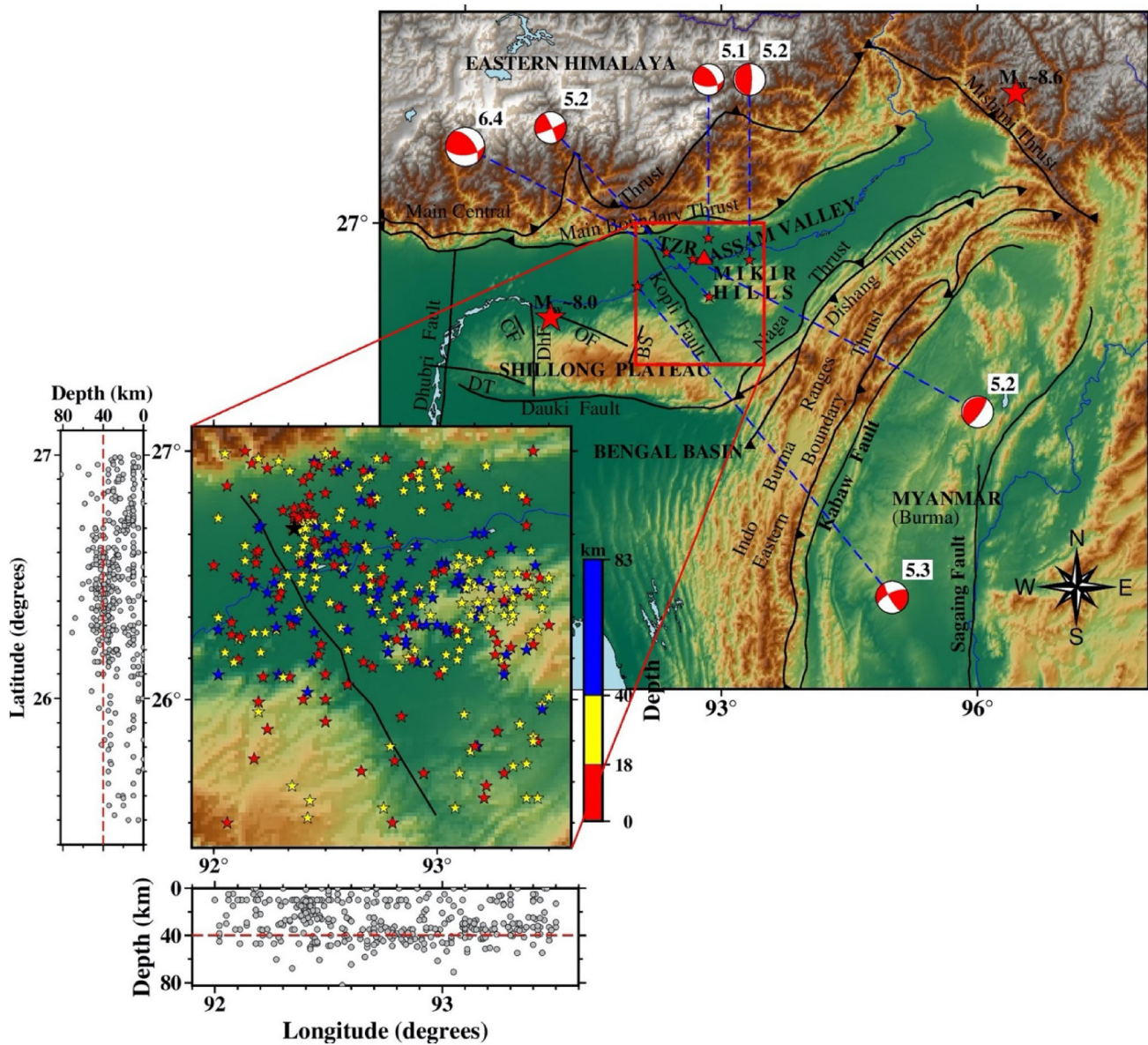


Figure 1. Major tectonic features in the study region. The broadband station TZR and two great earthquakes occurred in the region are marked by red triangle and red star, respectively. Earthquakes ( $>5.0$ ) along with their beach balls (red) around the Kopili Fault region are shown in red star. The inset figures show the seismicity plot in the Kopili region, as well as its projection latitudinally and longitudinally with the black star, denotes the recent earthquake ( $M_w = 6.5$ ; 2021/4/28) and red dashed line denotes the probable Moho (40 km). The colour scale shows the depth of the earthquakes in the region.

Dauki Fault to the south. To the west, the Plateau is delimited by the Dhubri Fault, which generated an earthquake of magnitude 7.1 in 1930. Bilham and England (2001) identified a hidden fault, named as Oldham Fault, to the northern boundary of the plateau, and they proposed that the great 1897 Shillong earthquake occurred by pop-up tectonics of the plateau between the south-dipping Oldham Fault and north-dipping Dauki Fault by reverse faulting. Tapponnier *et al.* (1982) suggested that active spreading of the Andaman Sea and lateral motion along the Sagaing Fault in

Myanmar are the reason for the formation of Assam syntaxis, where the great Assam earthquake occurred (Tapponnier *et al.* 1982).

There have been different opinions about the seismogenic strength of the continental lithosphere beneath the actively deforming continental region, including northeast India and Shillong Plateau. Molnar and Chen (1983, 1990) proposed that the seismogenic strength of the continental lithosphere either lie in the upper crust alone or in some regions both in the upper crust and in the upper mantle, while the lower crust is always weak and deforms

aseismically (Molnar and Chen 1983; Chen and Molnar 1990). Maggi *et al.* (2000a, b) found that in most of these regions, it was only the upper crust, and in some areas, the entire crust displayed seismogenic strength (Maggi *et al.* 2000a, b). Mitra *et al.* (2005) used receiver function derived velocity models and recomputed depths of earthquakes studied by Chen and Molnar (1990) and showed that all these earthquakes were in the lower crust and the entire crust beneath northeast India was seismogenic (Mitra *et al.* 2005).

The Kopili Fault, a 300-km long and 50-km wide transverse structure, links the two tectonic zones, *viz.*, the Bhutan Himalaya to the north and the Assam Valley to the south, is the most active fault that can be capable of generating more significant earthquakes in northeast India (Kayal *et al.* 2010). Now it is widely accepted that the Kopili Fault is the causative source for the 10th January 1869  $M$  7.5 Cachar earthquake and the 23rd October 1943  $M$  7.2 Assam Valley earthquake, which occurred at the southern and at the centre of the Kopili Fault, respectively, causing severe damage in northeast India (Nandy 2001; Kayal *et al.* 2010). Most recently, on 28th April 2021 at 7.21 AM IST, a strong earthquake of magnitude  $M_w$  6.5 at 20 km depth jolted northeast India, which was attributed to the Kopili Fault. This earthquake is the largest magnitude earthquake recorded near the Kopili Fault region after the 1943 earthquake (red box in figure 1). The focal mechanism solutions of earthquakes ( $M_w > 5$ ) from the Global CMT Project catalogue show that the region is dominated by low-angle reverse faulting, oblique faulting and strike-slip faulting. The epicentres of earthquakes (1964–2021) are shown in the inset of figure 1, illustrating depth-wise variation of earthquakes and their projections along longitudinal and latitudinal directions.

In the present study, crustal shear velocity structure near Kopili Fault is calculated by using receiver function modelling for station Tezpur (TZR). Taking into account the occurrence of the strong earthquake of magnitude 6.5 in the Kopili Fault region (Sonitpur district), we venture to study the temporal shift in the  $b$ -values before and after the mainshock and depth-wise variation of  $b$ -values. The results established in this paper smear a new viewpoint regarding earthquake precursor study and mitigation of seismic hazards. We also calculated temporal and depth-wise variation  $b$ -values in the region and checked their correlation with the crustal structure.

## 2. Data

To estimate the shear velocity crustal structure beneath station TZR, teleseismic earthquakes recorded during 2001–2007 were used. The station is operated by National Geophysical Research Institute (NGRI) Hyderabad and is equipped with CMG-3T seismometer and REFTEK data logger. The earthquake waveform data for TZR station are taken at sampling rates of 20 samples. For  $b$ -value calculation, earthquake catalogue for the period between 1964 and 2021 has been collected from the bulletin of International Seismological Centre (ISC) and National Centre for Seismology (NSC), avoiding any duplicacy. Overall, 380 events are taken into consideration in a rectangular region of  $1.5^\circ \times 1.5^\circ$  between  $25.5^\circ$ – $27^\circ$ N and  $92^\circ$ – $93.5^\circ$ E along the Kopili Fault region. Since the reported magnitude in the NSC is moment magnitude ( $M_w$ ), and in the ISC are  $M_w$ ,  $M_b$ ,  $M_s$ ,  $M_l$ , etc., magnitude conversion from  $M_b$ ,  $M_s$ ,  $M_l$ , etc., to  $M_w$  is done for ISC database to maintain homogeneity in magnitude.

## 3. Methodology

### 3.1 Receiver function calculation

Receiver function (RF) is a well-established seismological approach that has been used to image shear velocity structure beneath any station. When a seismic wave hits a discontinuity, along with reflection and refraction, P-to-S conversion (Ps) also occurs. By modelling the Ps and their multiples (multiple reflections within two layers), like PpPs and PpSs, which are the phases observed in the receiver function, can provide thicknesses and shear velocities ( $V_s$ ) of different layers beneath the station.

For RF calculation, earthquakes of magnitude  $\geq 5.0$  and epicentre distance between  $30^\circ$  and  $95^\circ$  with clear direct P-arrival on vertical component of seismogram are used that nullify the complexities occurred on P phase due to triplication and core-mantle phases. The horizontal component seismograms (N–S and E–W), which contain converted phases, are converted to radial and transverse components, respectively, by rotating the components with respect to the great circular path. The radial and transverse components of seismograms are deconvolved with the vertical component using iterative time-domain deconvolution method



(Ligorriá and Ammon 1999) to calculate radial RF (now onward only RF) and transverse RF, respectively. In this study, RF of  $G_w = 2.5$  is used, which corresponds to low pass filter of corner frequency 1.25. Figure 2 shows the RFs plotted with respect to back azimuth, where clean Ps are observed at 5 s and one multiple PpPs is observed at  $\sim 15$ –18 s; however, the second multiple (PpSs) is not clearly observed. To enhance Ps and PpPs phases, RFs are stacked in a narrow epicentre distance and back azimuths to get a single estimate

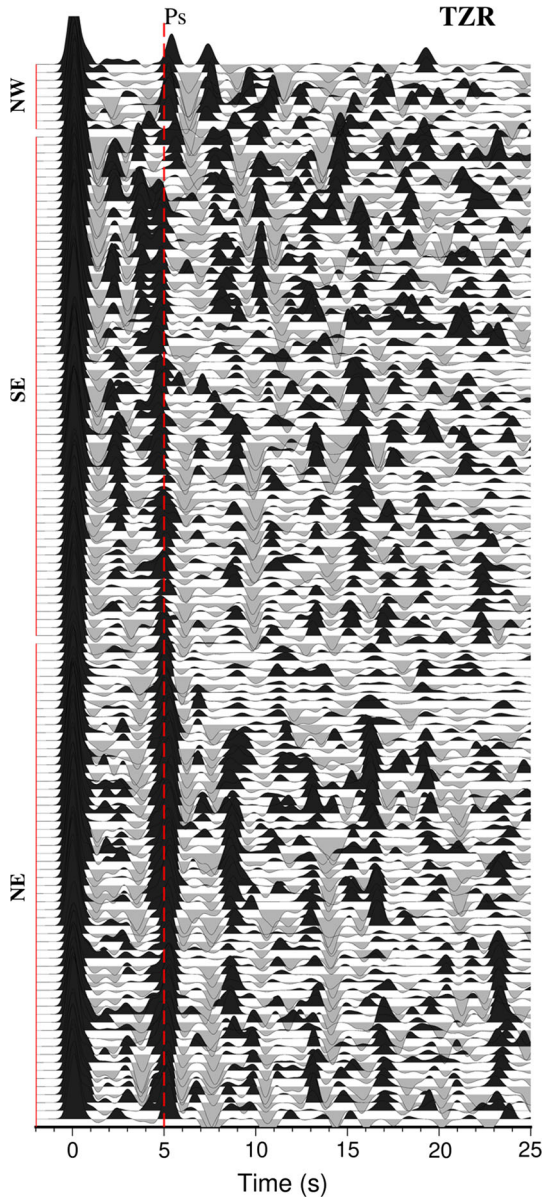


Figure 2. Receiver functions plotted with increasing back azimuth for the station TZR. P-to-S converted phase (Ps) is marked by red dashed line. Receiver functions in different back azimuths (NE, SE, SW, and NW) are shown by red vertical line.

of RF. One standard deviation ( $\pm 1\sigma$ ) error bounds of stacked RF are also calculated from the variance, which is used to check the RF fitting in RF inversion and in the estimation of uncertainties in  $V_s$  and thicknesses of layers.

### 3.2 Receiver function inversion

RFs are sensitive to velocity contrast across the layer and surface wave dispersion data provides absolute velocity in these layers. These two complementary nature datasets are jointly inverted by using iterative linearize damped least-square technique of Julià *et al.* (2000) and Herrmann and Ammon (2004) to get 1-D  $V_s$  model beneath a station. In this method 1-D velocity model is estimated by minimizing the objective function  $S$  (Julià *et al.* 2000; Herrmann and Ammon 2004), defined as:

$$S = \frac{1-p}{N_r} \sum_{a=0}^{N_r} \left( \frac{O_{ra} - P_{ra}}{\sigma_{ra}} \right)^2 + \frac{p}{N_s} \sum_{b=0}^{N_s} \left( \frac{O_{sb} - P_{sb}}{\sigma_{sb}} \right)^2, \quad (1)$$

where  $N_r$  and  $N_s$  are the total number of RF and the surface wave data point, respectively;  $O_{ra}$  and  $P_{ra}$  are the observed and predicted RF at time  $t_a$ ;  $O_{sb}$  and  $P_{sb}$  are the  $b$ th observed and predicted surface wave dispersion data; and  $\sigma_{ra}$  and  $\sigma_{sb}$  are the standard errors for RF and dispersion dataset. The *a-priori* factor  $p$  (lies between 0 and 1) is known as influence parameter that changes the influence of either dataset on the minimization procedure. In this study,  $p$  set to 0.5, which offers optimal balance to fit both the dataset. For inversion, a half-space initial model of  $V_s = 4.48$  km/s ( $V_p/V_s = 1.79$  and density =  $3.3$  gm/cm<sup>3</sup>) and layer thickness of 2 km is used. Rayleigh wave group velocity dispersion data between 10 and 70s are taken from a tomographic study carried out by Acton *et al.* (2010). The inversion is repeated 30 times to get the final  $V_s$  model. The  $V_s$  model generated through inversion is forward modelled by combining the adjoining layers of similar velocity to get the final realistic velocity model. Figure 3 demonstrates the joint inversion methodology for a stacked RF binned in epicentre distance (DEL)  $34^\circ$  and  $68^\circ$  and in back azimuth (BAZ)  $38^\circ$  and  $85^\circ$ , and group velocity dispersion data between 10 and 70s. Best fitted RF (figure 3a) and dispersion curves (figure 3b) correspond to  $V_s$  model generated through inversion and forward

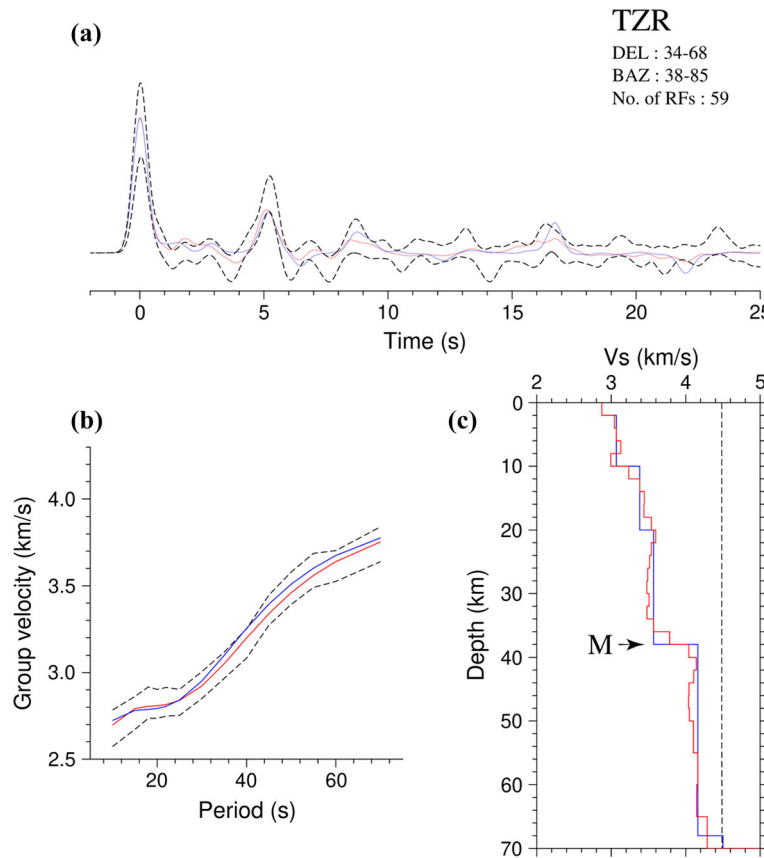


Figure 3. Joint inversion results for the station TZR in the NE back-azimuth. **(a)** Fitting of synthetic RF estimated from inversion (red colour) and forward modelling (blue colour) along with the error bound (black dashed lines). Station name, epicentral distance (DEL), back azimuth (BAZ) ranges, and number of receiver functions are also shown at the top right corner of the plot. **(b)** Fitting of synthetic dispersion curve estimated from inversion (red colour) and forward modelling (blue colour) along with the error bound (black dashed lines). **(c)** 1-D  $V_s$  model from inversion (red colour) and forward modelling (blue colour). Initial model is shown by black dashed line. Moho (M) is marked by black arrow.

modelling (figure 3c) are shown in red and blue colour, respectively. A significant velocity jump ( $\geq 4.2$  km/s) is observed at 38 km, which corresponds to Moho and is marked by black arrow. Moho depth is varied by  $\pm 1.0$ ,  $\pm 1.5$ , and  $\pm 2.0$  km to compute its uncertainties. The synthetic RF and dispersion curve produced by these models are then examined to see if they fall within the  $\pm 1\sigma$  error boundaries. We found 1.5 km is the error in Moho depth calculation. Same procedure is applied for the other stack RFs from the remaining back azimuths for the station TZR.

### 3.3 Magnitude conversion

The earthquakes catalogue collected from ISC and NEIC have different magnitude types, *viz.*, moment magnitude ( $M_w$ ), body wave magnitude ( $M_b$ ), surface wave magnitude ( $M_s$ ), local magnitude ( $M_l$ ), etc. Most of the earthquake information contains any of the four magnitude types  $M_w$ ,  $M_b$ ,

$M_s$  and  $M_l$  or their combination. We observed that most of the earthquakes from ISC catalogue and all the earthquakes collected from NSC catalogue have  $M_w$  information. To utilize more data in our calculation, we convert other magnitudes to  $M_w$  by estimating suitable relation. To establish relation between  $M_w$  and other magnitude scales, the Deming regression method (Jensen 2007) is used. Deming regression, also known as orthogonal regression, takes into consideration the measurement errors in both the predictor and the response. Since magnitudes are subject to measurement errors, use of Deming regression method is justified. The procedure is well explained in various literature (Kendall and Stuart 1968; Das *et al.* 2011; Wason *et al.* 2012). For our study, to establish the relations, we have taken into account earthquake data from the ISC catalogue for the period between 1964 and 21/6/2021 for the entire northeast region ( $90^\circ$ – $98^\circ$ E and  $22^\circ$ – $29^\circ$ N) as shown in figure 1. The estimation of parameters is done using the package Deming

regression of R software. The relation endorsed, as shown in figure 4 are as follows:

$$M_w = 1.10(\pm 0.07)M_b - 0.50(\pm 0.33), \quad (2)$$

$$M_w = 1.02(\pm 0.06)M_l - 0.09(\pm 0.22), \quad (3)$$

$$M_w = 0.84(\pm 0.10)M_s + 1.23(\pm 0.49). \quad (4)$$

### 3.4 *b*-value estimation

Several efforts have been made by researchers to map the frequency of earthquakes as a function of space, time and depth, and finally, Gutenberg and Richter (1954) entrenched the accord between occurrence-density ( $N$ ) and magnitude ( $M$ ) of earthquakes in a region for a specific time period (Gutenberg and Richter 1945). The frequency magnitude distribution (FMD) of earthquakes pursues a log-linear relationship given by:

$$\log_{10} N(M) = a - bM, \quad M \geq M_c, \quad (5)$$

where  $N(M)$  is the aggregate sum of earthquakes,  $M$  denotes magnitude and  $M_c$  is the magnitude of completeness below, which halts to show a linear trend with respect to due to scarce coverage inclusion (Wiemer and Wyss 2000). The intercept ‘ $a$ ’ portends the level of seismicity of a region, which confides in various factors such as duration of the study period, highest magnitude observed in the study period, and most importantly, size and stress zone of the region (Allen 1986). Mathematically, the constant  $b$  is patent as the  $b$ -value is the slope of equation (5), which implies the degree of decline in the occurrence of earthquakes with rising magnitudes.  $b$ -value can be inferred as a determining value for seismic characteristics of a region. Although, in a region that is signified as an active region, the  $b$ -value is  $\sim 1$ , but in most cases, we observed deviation from 1. This deviation can be

inferred as the occurrence of small magnitude earthquakes due to an increase in diversification of material composition or incremental crack density, which results in an increasing  $b$ -value (Kayal 2008; Wason *et al.* 2012) or lowering of  $b$ -values due to the rise of active stress in the region inkling of massive earthquakes (Wyss 1973). Predominantly,  $b$  is inferred as an indexing parameter for material heterogeneity and enforced shear stress, due to which it is important to investigate the temporal variation of  $b$ -value to mollify seismic hazard. The time dependency  $b$ -value may illustrate two laps. The rising lap indicates that the occurrence of smaller magnitude earthquakes is comparatively larger and the falling lap suggests that the occurrence of larger magnitude earthquakes is increasing. Imoto (1991) categorized the time dependency  $b$ -value into rise, fall, and no difference (Imoto 1991).

We have estimated  $M_c$  by maximum curvature method (MAXC) (Wiemer and Wyss 2000) and subsequently,  $b$ -value is estimated via the method of bootstrap regression (Efron and Tibshirani 1993, 1994; Efron 2007). The steps for bootstrap regression method are as follows:

- The regression coefficients  $a$  and  $b$  of equation (5) are estimated for the original sample and subsequently, fitted values ( $\log \widehat{N(M)}$ ) and residuals ( $r = \log(N(M)) - \log \widehat{N(M)}$ ) are calculated.
- For each bootstrap sample of residual  $R_i = [r_{i1}, r_{i2}, r_{i3}, \dots, r_{in}]'$ , bootstrapped values  $LOG_i = [LOG_{i1}, LOG_{i2}, LOG_{i3}, \dots, LOG_{in}]'$  are calculated, where  $LOG_{ij} = \log(\widehat{N(M)})_{ij} + r_{ij}$ ,  $N$  denotes the number of samples in the original sample and subscript  $i$  denotes  $i$ th bootstrapped sample.
- The obtained bootstrapped values  $LOG_i$  regressed on the fixed  $M$  values and  $\hat{a}_i$  and  $\hat{b}_i$  are obtained for the  $i$ th bootstrapped sample.

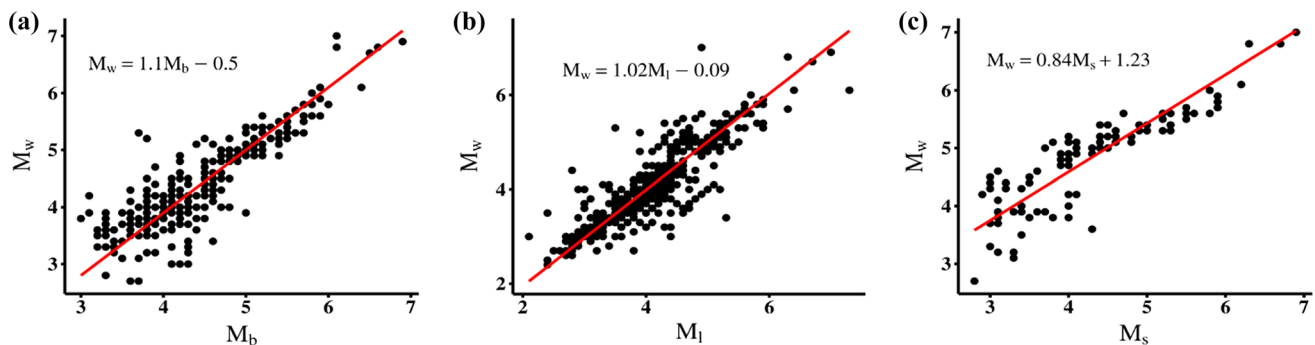


Figure 4. Regression fitting (red line) between the magnitudes (a)  $M_b$  and  $M_w$ , (b)  $M_l$  and  $M_w$ , and (c)  $M_s$  and  $M_w$ . Relations between the magnitudes are shown in the top left corner of each plot.

Suppose there are  $b$  bootstrapped samples, then we have  $B$  number of  $a$  and  $b$ -values.

- Using the distribution of  $\hat{b}_i$ , the estimator  $\hat{b}$  and standard error (SE) of  $\hat{b}$  are obtained as:

$$\hat{b} = \frac{\sum_{i=1}^B \hat{b}_i}{B}, \quad (6)$$

$$\text{SE}(\hat{b}) = \sqrt{\frac{\sum_{i=1}^B (\hat{b}_i - \hat{b})^2}{B - 1}}. \quad (7)$$

To get an overall estimate of  $b$ -value in the region, we took a period from 1964 and 2021, which includes around 380 earthquakes. At first histogram-density plot of the magnitude of earthquakes is obtained, as shown in figure 5(a) to get an overview of the distribution of the earthquakes. Although the distribution is almost normal, since the data has a lower bound zero, it is relatively skewed right. Since the skewness is very low, we assumed the distribution to be normal. Secondly, for the given period, we marked the threshold magnitude  $M_c$  at 3.3 via the maximum curvature method. We estimated  $b$  and its error bar via bootstrap regression method as discussed above, as shown in figure 5(b) and found the  $b$ -value as 0.94 with an uncertainty of 0.14. For the temporal variation of  $b$ -values and to check the variation of  $b$ -values just before and after the massive earthquake, we selected the time window in such a way as to keep a constant length of events around 60 for each time window. For those time windows, where maintaining constant event length was difficult, we considered overlapping of events from the previous time window. Subsequently, we estimated  $M_c$  for each time window via the maximum curvature

method and estimated  $b$  through the bootstrap regression method. Similarly, we estimated  $b$ -values with respect to depth following the above-mentioned procedure.

#### 4. Results and discussions

Inversion modelling results for the station TZR from different back azimuths are shown in figures 3, 6, and 7. Shear velocity structure beneath TZR in the NE back azimuth is investigated by modelling stack RF calculated from 59 RFs in the  $38^\circ$ – $85^\circ$  back azimuths. Modelling results in the NE back azimuths show 38 km thick crust, which includes 20 km upper crust ( $V_s \leq 3.5$  km/s) followed by 18 km lower crust ( $V_s > 3.5$  km/s). Shear velocity structure in the SE back azimuths is estimated in four stack blocks. Crustal thickness in most of the blocks shows 40 km thick crust with 18 km upper crust and 22 km lower crust. RF modelling in the  $115^\circ$ – $137^\circ$  back azimuth shows 35 km crust with 18 km upper crust, which provides the structure beneath Mikir Hills. No suitable RFs are found from the SW back azimuth. Shear velocity structure beneath NW back azimuth is observed to be similar to NE and SE back azimuths. The crust is 40 km thick with 20 km thick upper and lower crust. Upper mantle shear velocity is observed to be 4.2 km/s beneath TZR station. Similar crustal structure had been observed in the previous receiver function studies in northeast India (Bora *et al.* 2016; Borah *et al.* 2016).

Seismicity map, earthquakes depth-wise variation map and projection of earthquakes in longitudinally and latitudinally along the Kopili Fault

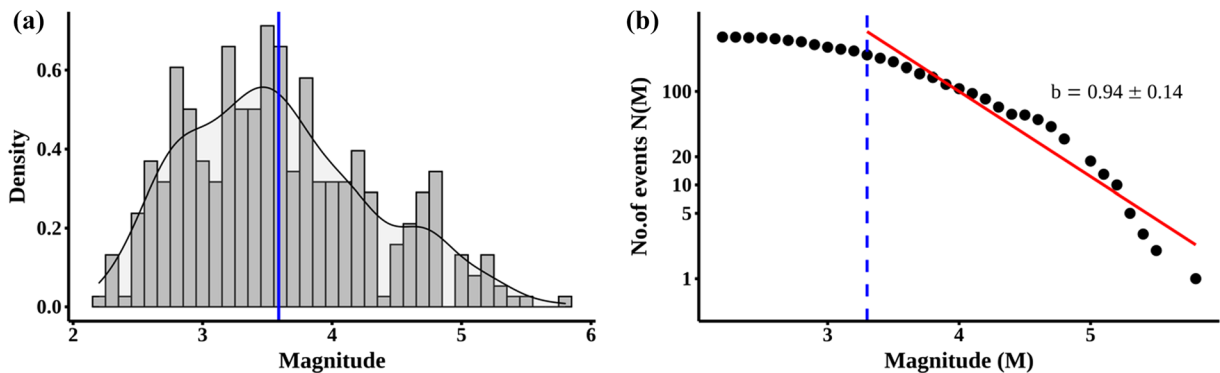


Figure 5. (a) Histogram density plot of magnitude of earthquakes in the time period between 1964/1/1 and 2021/6/22 with blue solid line depicting the average magnitude of the incomplete catalogue. (b)  $\log(N(M))$  vs.  $M$  plot for the specified time period. Blue dashed vertical line indicates  $M_c = 3.3$  value and red line indicates the regression fitting between  $\log(N(M))$  and  $M$ .  $b$ -value with error is also shown in the top right corner of the figure.



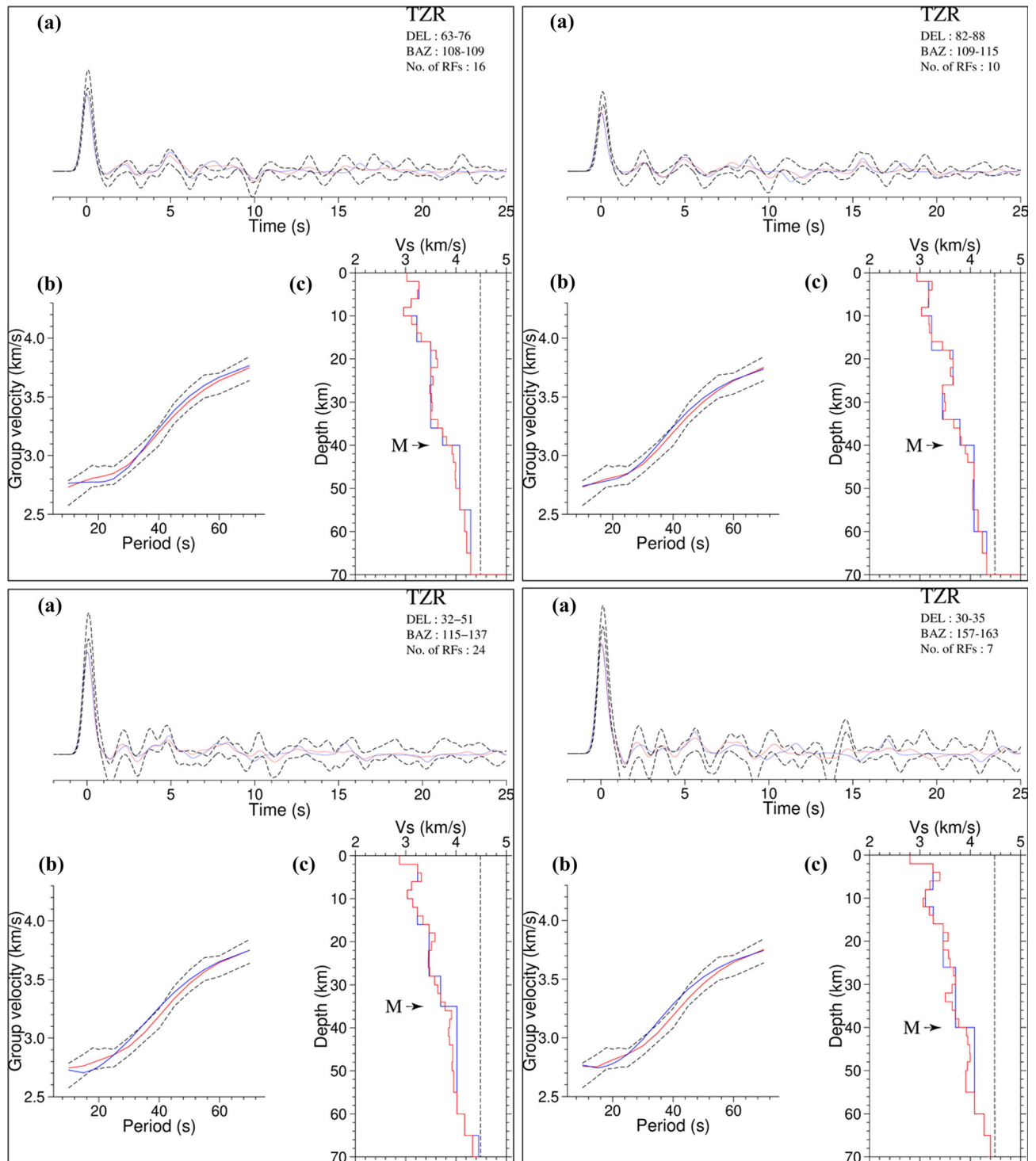


Figure 6. Joint inversion results for the station TZR in the SE back azimuth. Other details are the same as in figure 3.

show that all earthquakes occur in both crust and the upper mantle (figure 1). It has been seen in the projected plots that most of the earthquakes are aggregated near the Moho (40 km) as well as in the upper crust and in the upper mantle, which suggests that both crust and the upper mantle along the Kopili Fault are seismogenic. The overall

$b$ -value of the Kopili region is estimated to be 0.94. To check the temporal variation of  $b$ -value, the earthquake catalogue during the period between 2010/1/1 and 2021/6/21 has been taken and subdivided into five-time windows. In each time window, there are  $\sim 60$  data points and in those time windows, where there are fewer data points



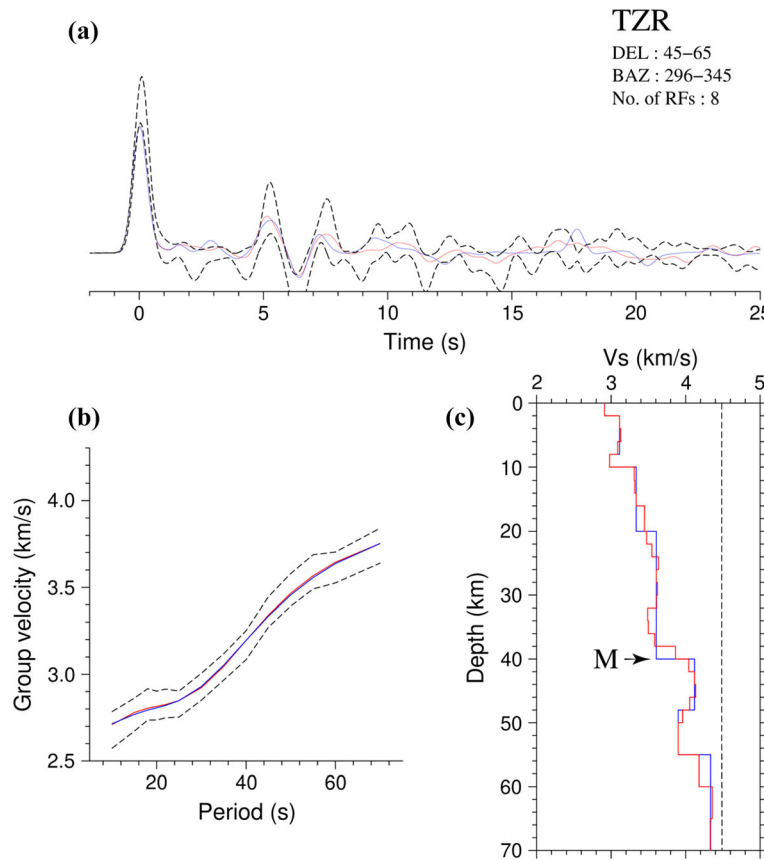


Figure 7. Joint inversion results for the station TZR in the NW back azimuth. Other details are the same as in figure 3.

overlapping with the preceding time window is done to maintain uniformity in the number of data points. The  $b$ -value for each time window is estimated via bootstrap regression method as discussed above. The results show  $b$ -value is  $\sim 1$  between 1964/1/1 and 2018/12/31 (figure 8). Sudden decrease of  $b$ -value (0.76) is observed in the time window 2019/1/1 and 2021/4/27. Interestingly, the sudden drop of  $b$ -value is observed in the time window 2019/1/1 and 2021/4/27 just before the 28th April 2021  $M_w$  6.5 Sonitpur earthquake (red star in figure 9). According to a hypothesis by Main *et al.* (1989), the abrupt change in  $b$  value due to a large earthquake should crop up at  $b = 0.5$  (Main *et al.* 1989). Due to the earthquake that took place on 2021/4/28, we noticed this abrupt change in  $b$ -value in the preceding time duration. Previous studies in different regions over the globe show an abrupt fall in  $b$ -value prior to a massive earthquake (Smith 1986; Nuannin *et al.* 2005; Khan *et al.* 2011; Borgohain *et al.* 2018). A study on the temporal deviation of  $b$ -values is made by Hirose *et al.* (2002) in the subduction zone and observed an unforeseen change in the rate of change of  $b$ -value. Change in the  $b$ -value estimate from 1.2 to 0.7 just ahead of

$M = 6.2$  Northern Miyagi, Japan, earthquake, 2003 is proclaimed by Tsukakoshi and Shimazaki (2008). Sharma *et al.* (2013) and Bora *et al.* (2018) reported low  $b$  values differing from 1.4 to 0.9 ahead of a massive deep earthquake at the Indo-Burma subduction zone. Rehman *et al.* (2015) computed temporal variation of  $b$ -value in Hazara region (Pakistan) and they found a significant decrease of  $b$ -value prior to 8th October 2005 Kashmir earthquake ( $M_w = 7.6$ ) (Rehman *et al.* 2015). Numerical simulations and laboratory experiments have also given affirmation on low  $b$ -values prior to great earthquakes (Scholz 1968; Sammonds *et al.* 1992; Hainzl *et al.* 2003; Lei *et al.* 2004). Although we have not observed any significant rise in  $b$ -value just after the earthquake, as shown in figure 8, as small time window has been used for  $b$ -value estimation in that duration.

RF modelling results beneath station TZR show a 40 km crust with 18–20 km upper crust followed by 20 km thick lower crust. So, in this study, we have estimated  $b$ -values in the upper crust, lower crust and upper mantle, as shown in figure 10. The results show  $b$ -value in upper crust, lower crust and upper mantle are 0.6, 0.8 and 1, respectively. The

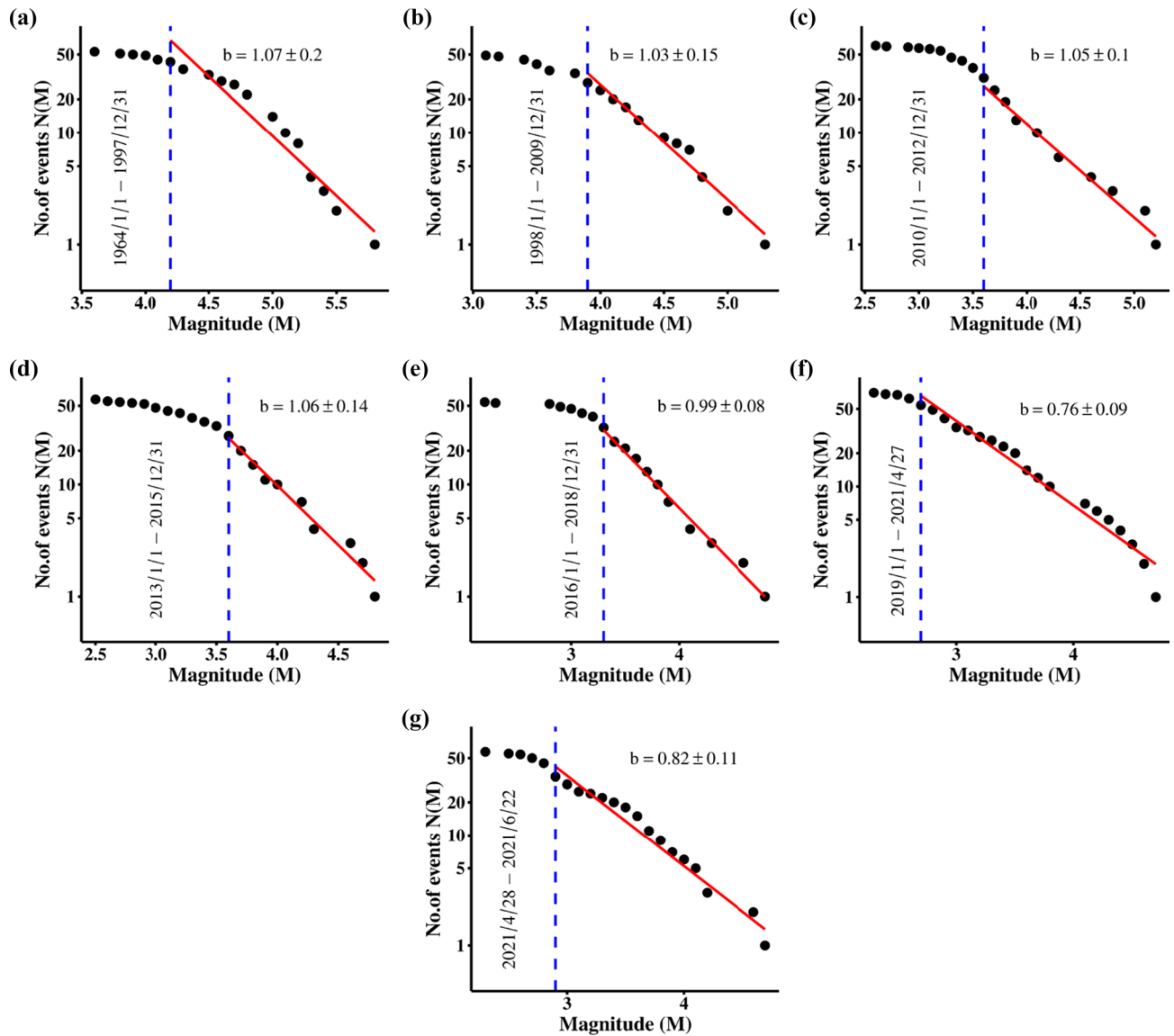


Figure 8.  $\log(N(M))$  vs.  $M$  plot for different time periods between 1964/1/1 and 2021/6/22. Other details are the same as in figure 5.

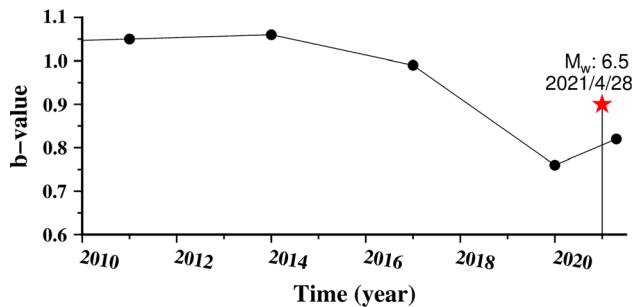


Figure 9. Temporal variation of  $b$ -value (black circle) between 2010 and 2021. The earthquake of magnitude  $M_w: 6.5$  is marked by red star.

observed changes in the  $b$ -value in upper-lower crust and upper mantle may be due to the increase in the strength of crust–upper mantle material

caused by the growth in temperature and pressure in depth ranges from 0 to 55 km.

Moreover, to check the variation of  $b$ -value with depth, we have calculated  $b$ -values at every 10 km depth interval from the surface with 5 km overlapping, down to 55 km depth, and finally plotted  $b$ -values with respect to average depth in those depth intervals (figure 11). Although earthquakes are also found at deeper depths ( $>55$  km), the quantity is very low. So, these data are not used for depth-wise calculation of  $b$ -values. We observed that  $b$ -values increase with depth, as shown in figure 11. Depth-wise variation of  $b$ -value gives stress accretion sorting at various depths. Results also show that down to 40 km depth,  $b$ -value is less than 1, which illustrates that larger earthquakes

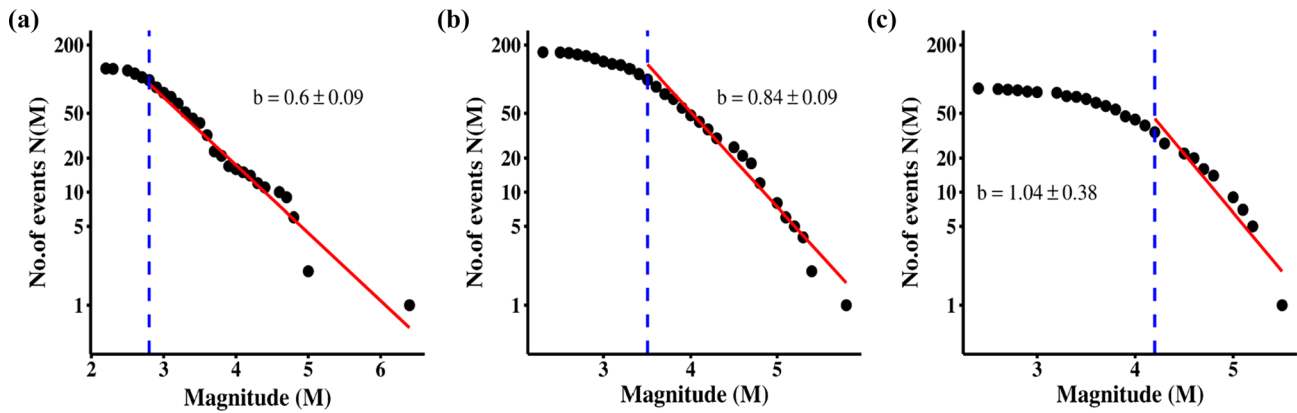


Figure 10.  $\log(N(M))$  vs.  $M$  plots of various depth ranges: (a) 0–18 km, (b) 18–40 km and (c) >40 km. Other details are the same as in figure 5.

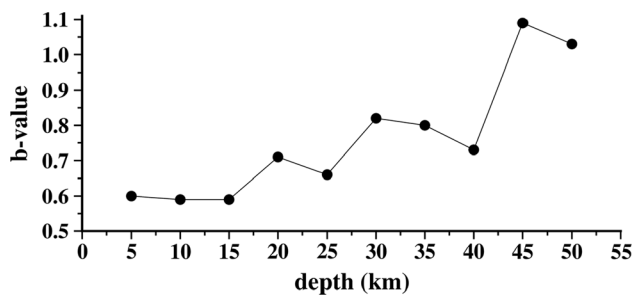


Figure 11. Depth-wise variation of  $b$ -value (black circle) in the study region.

monopolize over smaller earthquakes in that region. Moreover, the recently observed large earthquake ( $M_w \sim 6.5$ ) has a depth of around 17 km. Below 40 km, the  $b$ -value is observed to be  $>1$  and most interestingly, 40 km marks the most probable crust–mantle transition zone as observed from receiver function modelling. From figure 1, in the projected plots, it is observed that most of the earthquakes are accumulated within the crust–mantle transition zone. This rise in  $b$ -value is a clear indication of normal stress reduction at deeper depths. Hence,  $b$ -values can also be used for detecting primary discontinuities. Similar correlation of abrupt increase  $b$ -value with Moho is also observed in the Indo-Burma range (Bora *et al.* 2018).

## 5. Conclusions

We have calculated crustal structure and  $b$ -value in the Kopili Fault region, using joint inversion modelling of receiver function and surface wave data, and using Gutenberg–Richter relation, respectively. Results show that crust beneath the Kopili Fault region is 40 km thick and  $b$ -value is

0.9 in the region. We observed a clear correlation between abrupt increases in  $b$ -value with the Moho discontinuity. We also observed a reduction of  $b$ -value prior to the 28th April 2021  $M_w$  earthquake. So,  $b$ -value estimation can provide useful information in imaging crust–upper mantle discontinuities and earthquake precursor studies.

## Acknowledgements

Teleseismic data obtained from National Geophysical Research Institute (NGRI), Hyderabad is acknowledged. Most of the data processing was done using Seismic Analysis Code (SAC) and R software and figures were made using Generic Mapping Tools (GMT) and R software. The comments from two anonymous reviewers are constructive and valuable that greatly improved the manuscript. We are grateful to Prof. Charles Ammon and Malcolm Sambridge for making their receiver function calculation and inversion modelling code available. B Sarma and Anand are grateful to INSPIRE fellowship for supporting the study. K Borah acknowledges Academic Research Funding (ARF) from IISER Kolkata. This study has been supported by a grant from the Science & Engineering Research Board (MTR/2019/001260 and CRG/2020/003726).

## Author statement

Banashree Sarma: Data curation, modelling, writing – original draft preparation; Kajaljyoti Borah: Conceptualization, writing – reviewing and editing; Dipok K Bora: Reviewing and editing; and Aakash Anand: Methodology.

## References

- Allen J R L 1986 Earthquake magnitude-frequency, epicentral distance, and soft-sediment deformation in sedimentary basins; *Sedim. Geol.* **46**, [https://doi.org/10.1016/0037-0738\(86\)90006-0](https://doi.org/10.1016/0037-0738(86)90006-0).
- Ambraseys N N and Douglas J 2004 Magnitude calibration of north Indian earthquakes; *Geophys. J. Int.* **159**, <https://doi.org/10.1111/j.1365-246X.2004.02323.x>.
- Bilham R and England P 2001 Plateau 'pop-up' in the great 1897 Assam earthquake; *Nature* **410**, <https://doi.org/10.1038/35071057>.
- Bora D K, Borah K and Goyal A 2016 Crustal shear-wave velocity structure beneath Sumatra from receiver function modelling; *J. Asian Earth Sci.* **121**, <https://doi.org/10.1016/j.jseaes.2016.03.007>.
- Bora D K, Borah K, Mahanta R and Borgohain J M 2018 Seismic *b*-values and its correlation with seismic moment and Bouguer gravity anomaly over Indo-Burma ranges of northeast India: Tectonic implications; *Tectonophysics*. **728** 130–141, <https://doi.org/10.1016/j.tecto.2018.01.001>.
- Borah K, Bora D K, Goyal A and Kumar R 2016 Crustal structure beneath northeast India inferred from receiver function modelling; *Phys. Earth Planet. Int.* **258**, <https://doi.org/10.1016/j.pepi.2016.07.005>.
- Borgohain J M, Borah K, Biswas R and Bora D K 2018 Seismic *b*-value anomalies prior to the 3rd January 2016,  $M_w = 6.7$  Manipur earthquake of northeast India; *J. Asian Earth Sci.* **154**, <https://doi.org/10.1016/j.jseaes.2017.12.013>.
- Das R, Wason H R and Sharma M L 2011 Global regression relations for conversion of surface wave and body wave magnitudes to moment magnitude; *Nat. Hazards* **59**, <https://doi.org/10.1007/s11069-011-9796-6>.
- Efron B 2007 Bootstrap methods: Another look at the Jackknife; *Ann. Stat.* **7**, <https://doi.org/10.1214/aos/1176344552>.
- Efron B and Tibshirani R J 1993 An Introduction to the Bootstrap; Monographs on Statistics and Applied Probability 57, Springer Science+Business Media Dordrecht.
- Efron B and Tibshirani R J 1994 An Introduction to the Bootstrap; Chapman and Hall, 456p.
- Gutenberg B and Richter C F 1945 Seismicity of the earth; *Bull. Geol. Soc. Am.* **56**, [https://doi.org/10.1130/0016-7606\(1945\)56\[603:SOTE\]2.0.CO;2](https://doi.org/10.1130/0016-7606(1945)56[603:SOTE]2.0.CO;2).
- Hainzl S, Zöller G and Scherbaum F 2003 Earthquake clusters resulting from delayed rupture propagation in finite fault segments; *J. Geophys. Res.: Solid Earth* **108**, <https://doi.org/10.1029/2001jb000610>.
- Herrmann R B and Ammon C J 2004 Surface waves, receiver functions and crustal structure. Computer Programs in Seismology, VERSION 3.30, Saint Louis University.
- Hirose F, Nakamura A and Hasegawa A 2002 *b*-value variation associated with the rupture of asperities: Spatial and temporal distributions of *b*-value east off NE Japan; *Zisin (J. Seismol. Soc. Japan)* **55**, [https://doi.org/10.4294/zisin1948.55.3\\_249](https://doi.org/10.4294/zisin1948.55.3_249).
- Imoto M 1991 Changes in the magnitude-frequency *b*-value prior to large ( $M \geq 6.0$ ) earthquakes in Japan; *Tectonophysics*. **193**, [https://doi.org/10.1016/0040-1951\(91\)90340-X](https://doi.org/10.1016/0040-1951(91)90340-X).
- Jensen A C 2007 Deming regression. Technical Report, Vignette for the MethComp package for R, <http://staff.pubhealth.ku.dk/~bxc/MethComp/Deming.pdf>.
- Julia J, Ammon C J, Herrmann R B and Correig A M 2000 Joint inversion of receiver function and surface wave dispersion observations; *Geophys. J. Int.* **143**, <https://doi.org/10.1046/j.1365-246X.2000.00217.x>.
- Kayal J R 2008 *Microearthquake seismology and seismotectonics of South Asia*; Springer co-published with Capital Publishing Company, 447p.
- Kayal J R, Arefiev S S, Baruah S, Tatevossian R, Gogoi N, Sanoujam M, Gautam J L, Hazarika D and Borah D 2010 The 2009 Bhutan and Assam felt earthquakes ( $M_w$  6.3 and 5.1) at the Kopili Fault in the northeast Himalaya region; *Geomatics, Natural Hazards and Risk* (**3**), <https://doi.org/10.1080/19475705.2010.486561>.
- Kendall M G and Stuart A 1968 The advanced theory of statistics; *The Statistician* **18**, <https://doi.org/10.2307/2986781>.
- Khan P K, Ghosh M, Chakraborty P P and Mukherjee D 2011 Seismic *b*-value and the assessment of ambient stress in northeast India; *Pure Appl. Geophys.* **168**, <https://doi.org/10.1007/s00024-010-0194-x>.
- Lei X, Masuda K, Nishizawa O, Jouniaux L, Liu L, Ma W, Satoh T and Kusunose K 2004 Detailed analysis of acoustic emission activity during catastrophic fracture of faults in rock; *J. Struct. Geol.* **26**, [https://doi.org/10.1016/S0191-8141\(03\)00095-6](https://doi.org/10.1016/S0191-8141(03)00095-6).
- Ligorria J P and Ammon C J 1999 Iterative deconvolution and receiver-function estimation; *Bull. Seismol. Soc. Am.* **89** 1395–1400, <https://doi.org/10.1785/BSSA0890051395>.
- Maggi A, Jackson J A, McKenzie D and Priestley K 2000a Earthquake focal depths, effective elastic thickness, and the strength of the continental lithosphere; *Geology* **28**, [https://doi.org/10.1130/0091-7613\(2000\)028<0495:efdeet>2.3.co;2](https://doi.org/10.1130/0091-7613(2000)028<0495:efdeet>2.3.co;2).
- Maggi A, Jackson J A, Priestley K and Baker C 2000b A reassessment of focal depth distributions in southern Iran, the Tien Shan and northern India: Do earthquakes really occur in the continental mantle?; *Geophys. J. Int.* **143**, <https://doi.org/10.1046/j.1365-246X.2000.00254.x>.
- Main I G, Meredith P G and Jones C 1989 A reinterpretation of the precursory seismic hazard analysis; *Bull. Seismol. Soc. Am.* **85** 1299–1308.
- Mitra S, Priestley K, Bhattacharyya A K and Gaur V K 2005 Crustal structure and earthquake focal depths beneath northeastern India and southern Tibet; *Geophys. J. Int.* **160**, <https://doi.org/10.1111/j.1365-246X.2004.02470.x>.
- Molnar P and Wang-Ping Chen 1983 Focal depths and fault plane solutions of earthquakes under the Tibetan plateau; *J. Geophys. Res.* **88**, <https://doi.org/10.1029/JB088iB02p01180>.
- Nandy D R 2001 Geodynamics of the northeastern India and the adjoining region; *J. Geol. Soc. India* **91**(2) 248.
- Nuannin P, Kulhanek O and Persson L 2005 Spatial and temporal *b* value anomalies preceding the devastating off coast of NW Sumatra earthquake of December 26, 2004; *Geophys. Res. Lett.* **32**, <https://doi.org/10.1029/2005GL022679>.
- Rehman K, Ali A, Ahmed S, Ali W, Ali A and Khan M Y 2015 Spatio-temporal variations of *b*-value in and around north Pakistan; *J. Earth Syst. Sci.* **124**, <https://doi.org/10.1007/s12040-015-0625-2>.
- Sammonds P R, Meredith P G and Main I G 1992 Role of pore fluids in the generation of seismic precursors to shear fracture; *Nature* **359**, <https://doi.org/10.1038/359228a0>.



- Scholz C H 1968 The frequency–magnitude relation of microfracturing in rock and its relation to earthquakes; *Bull. Seismol. Soc. Am.* **58** 399–415, <https://doi.org/10.1785/BSSA0580010399>.
- Sharma S, Baruah S, Sahu O P, Bora P K and Duarah R 2013 Low *b*-value prior to the Indo-Myanmar subduction zone earthquakes and precursory swarm before the May 1995 M 6.3 earthquake; *J. Asian Earth Sci.* **73**, <https://doi.org/10.1016/j.jseaes.2013.04.019>.
- Smith W D 1986 Evidence for precursory changes in the frequency-magnitude *b*-value; *Geophys. J. Roy. Astron. Soc.* **86**, <https://doi.org/10.1111/j.1365-246X.1986.tb00662.x>.
- Tapponnier P, Peltzer G, le Dain A Y, Armijo R and Cobbold P 1982 Propagating extrusion tectonics in Asia: New insights from simple experiments with plasticine; *Geology* **10**, [https://doi.org/10.1130/0091-7613\(1982\)10<611:PETIAN>2.0.CO;2](https://doi.org/10.1130/0091-7613(1982)10<611:PETIAN>2.0.CO;2).
- Tsukakoshi Y and Shimazaki K 2008 Decreased *b*-value prior to the M 6.2 Northern Miyagi, Japan, earthquake of 26 July 2003; *Earth Planets Space* **60**, <https://doi.org/10.1186/BF03352847>.
- Wang-Ping Chen and Molnar P 1990 Source parameters of earthquakes and intraplate deformation beneath the Shilong Plateau and the northern Indoburman ranges; *J. Geophys. Res.* **95**, <https://doi.org/10.1029/jb095ib08p12527>.
- Wason H R, Das R and Sharma M L 2012 Magnitude conversion problem using general orthogonal regression; *Geophys. J. Int.* **190**, <https://doi.org/10.1111/j.1365-246X.2012.05520.x>.
- Wiemer S and Wyss M 2000 Minimum magnitude of completeness in earthquake catalogs: Examples from Alaska, the Western United States, and Japan; *Bull. Seismol. Soc. Am.* **90**, <https://doi.org/10.1785/0119990114>.
- Wyss M 1973 Towards a physical understanding of the earthquake frequency distribution; *Geophys. J. Roy. Astron. Soc.* **31**, <https://doi.org/10.1111/j.1365-246X.1973.tb06506.x>.

Corresponding editor: ARKOPROVO BISWAS